High–precision determination of carbon stable isotope in silicate glasses by secondary ion mass spectrometry: Evaluation of international reference materials

Hyunjoo Lee[a,*], Yves Moussallam[a,b], Estelle F. Rose−Koga[c], Laurette Piani[d], Johan Villeneuve[d], Nordine Bouden[d], Andrey A. Gurenko[d], Brian Monteleone[e], Glenn A. Gaetani[e]

[a] *Lamont−Doherty Earth Observatory, Columbia University, New York, USA*

[b] *American Museum of Natural History, Department of Earth and Planetary Sciences, NY 10024, New York, USA*

[c] *ISTO, UMR 7327, Université d'Orléans−CNRS−BRGM, 1A rue de la Férollerie, 45071 Orléans cedex 2, France*

[d] *Centre de Recherches Pétrographiques et Géochimiques (CRPG), UMR 7358, CNRS−UL 15 rue Notre Dame des Pauvres, 54500 Vandœuvre−lès−Nancy, France*

[e] *Dept Geology and Geophysics, Woods Hole Oceanographic Institution, Woods Hole, MA 02543, USA*

Corresponding author: Hyunjoo Lee; hl3507@columbia.edu

Abstract

Secondary ion mass spectrometry (SIMS) has been used for isotope analysis of volatile components dissolved in silicate melts for decades. However, carbon *in situ* stable isotope analysis in natural silicate glasses has remained particularly challenging, with the few published attempts yielding high uncertainties. In this context, we characterized 31 reference silicate glasses of basaltic and basanitic compositions, which we then used as reference materials to calibrate δ^{13}C−value analyses in silicate glasses by SIMS. This set of reference materials covers a wide range of CO_2 concentrations (380 ppm – 12000 ppm) and δ^{13}C values (-28.1 ± 0.2 to -1.1 ± 0.2‰, $\pm1\sigma$). The sets of reference materials were analyzed using large−geometry SIMS at two ion microprobe facilities to test reproducibility across different instrumental setups. The instrumental mass fractionation (IMF) varied widely with two different large−geometry SIMS instruments as well as with different analytical parameters such as field aperture size and primary beam intensity. We found that a precision better than ±1.1‰ (both average internal and external precision, ±1σ) for CO_2 content higher than 1800 ppm could be achieved using a primary beam intensity of less than 5nA, resulting in a final spot size of 10–20μm, allowing precise analysis of $\delta^{13}C$ in mineral−hosted melt inclusions. This level of precision was achieved at CO_2 concentrations as low as 1800 ppm. This advance opens a wide range of new possibilities for the study of $\delta^{13}C$−value in mafic melts and their mantle sources. The reference materials are now available at the CNRS–CRPG ion microprobe facility in Nancy, France and will be deposited at the Smithsonian National Museum of Natural History, Washington, USA where they will be freely available on loan to any researcher.

Keywords: SIMS; Ion probe; Carbon isotopes; $\delta^{13}C$−value; CO_2

1. Introduction

The measurement of the isotopic compositions of volatile species, such as δ^2H, $\delta^{13}C$, $\delta^{34}S$, and $\delta^{37}Cl$, in silicate glass has typically been performed by bulk rock analysis, such as vacuum extraction or elemental analyzer coupled to mass spectrometry (e.g., Sakai et al., 1982 for S; Ihinger et al., 1994 for general review; Barnes and Sharp, 2006 for Cl; Cartigny et al., 2008 for CO_2; Loewen et al., 2019 for H_2O). However, analysis at low volatile concentrations and isotope compositions in silicate glass by bulk extraction requires up to several hundred milligrams of material, which is challenging when sample availability is limited. In addition, bulk analyses of low volatile concentrations risk contamination by several unwanted materials such as seawater altered material (e.g., Cocker et al., 1982), adsorbed volatiles (e.g., Barker and Torkelson, 1975), organic impurities (e.g., Mattey et al., 1984), precipitated carbonate or reduced carbon on the vesicle wall (e.g., Mathez and Delaney, 1981), and CO_2 gas in micro−vesicles (e.g., Pineau and Javoy, 1983).

Secondary ion mass spectrometry (SIMS) is an *in situ* micro−analytical technique combining high spatial resolution with high sensitivity that is particularly well suited for determining the concentrations and isotopic compositions of light elements (H, Li, B, C, N, O, S) while overcoming many of the challenges involved with bulk analyses. Despite extensive efforts to analyze the isotopic compositions of volatiles in volcanic glasses such as hydrogen (e.g., Hauri et al., 2002, 2006), sulfur (e.g., Shimizu et al., 2019), and chlorine (e.g., Manzini et al., 2017) by the latest generation of SIMS, carbon isotopes have been largely ignored following earlier attempts (Hauri et al., 2002) due to its high background signal (e.g., Ihinger et al., 1994). In addition, the matrix effect for carbon isotope that affects the accuracy of SIMS measurements (e.g., Hauri et al., 2002) remains largely unexplored.

This paper presents new sets of reference materials for calibrating the measurement of isotopic composition and concentration of carbon in mafic silicate glasses over a wide range of carbon isotope ratios and concentrations. We detail the methods used to achieve improved internal precision and reproducibility (down to ±0.3‰, 1σ), allowing analysis of carbon isotopes at the 10μm scale. We evaluate the validity of the technique and reference materials, investigate compositional matrix effects, and perform test−measurements of carbon isotope on samples of known composition.

2. Methods

High pressure experiments were conducted using a piston cylinder. Carbon isotopic composition of the fused glasses was determined by an elemental analyzer coupled to isotope ratio mass spectrometry (EA−IRMS), while H_2O and CO_2 concentrations were quantified by Fourier Transform Infrared Spectroscopy (FTIR) at Lamont−Doherty Earth Observatory (USA). The major element compositions were measured by electron microprobe at the American Museum of Natural History (USA).

2.1. Samples

Three different subsets of synthetic silicate glasses were created: 1) mid−ocean ridge basalt (MORB), 2) Basanite, and 3) NBO (see below for explanation). A natural mid−ocean ridge basalt was used as starting material for the MORB series. We used the sample EDUL_DR75_1_04 (CNRS 000 000 2592) presenting a pillow basalt dredged from the South West Indian Ridge (SWIR) collected at 2650–2900 mbsl (meters below sea level) at 37°51′48″S, 49°20′12″E (https://lithotheque.ipgp.fr/edul.html). The initial composition is 50.1wt% SiO_2, 1.42wt% TiO_2, 16.4wt% Al_2O_3, 10.5wt% FeO_t, 0.2wt% MnO, 7.0wt% MgO, 11.4wt% CaO, 2.4wt% Na_2O, 0.2wt% K_2O, and 0.1wt% P_2O_5 (Moussallam et al., 2023).

As a starting material for the Basanite series, we used a natural basanite from El Hierro. The sample is a seawater quenched lava balloon, erupted at 100–300 m water depth, and collected at Lat: 27.697°, Lon: 17.993° in 2011–2012 (Longpré et al., 2017). The initial composition is 44.4wt% SiO_2, 5.0wt% TiO_2, 13.7wt% Al_2O_3, 12.5wt% FeO_t, 0.2wt% MnO, 8.1wt% MgO, 10.7wt% CaO, 3.5wt% Na_2O, 1.4wt% K_2O, and 0.5wt% P_2O_5 (Moussallam et al., 2019).

The NBO series glasses range in compositions from andesite to basalt, having been produced by high−pressure experiments by Lee et al. (2024). A mixture of the El Hierro basanite with varying amounts of SiO_2 and Al_2O_3 powders was used as the starting material.

Other reference materials, hereafter referred to as test glasses hereafter to be validated for IMF correction include a natural MORB (sample DR52; Maevaray, 2017) and additional synthetic glasses (ETNA−glass series and Hawaii−glass; Lee et al., 2024). DR52 is a basalt collected from SWIR at a depth of 3550m at 33.79°E, 56.13°S. The ETNA−glass series and the Hawaii−glass used basalt from Mt. Etna and the Hawaiian volcano, respectively, as starting materials. The ETNA−glass series and Hawaii−glass were synthesized in the same way as the NBO series, and detailed starting materials, experimental, and analytical methods for the NBO series, ETNA−glass, and Hawaii−glass can be found in Lee et al. (2024).

2.2. Experimental methods

To ensure homogeneity and remove pre−existing volatile components from the starting material, the starting powders for each series of glasses were placed in a platinum crucible, melted in a furnace at 1 atmosphere (0.1 MPa) and 1350°C for 2 hours and quenched. The resulting glass was then crushed and subjected to another melting cycle under identical conditions for an additional 2 hours. The loss of iron during melting was found to be insignificant, as the iron composition between the starting material (see 2.1) and the material after the experiment (Table 1) fell within the error range of the electron microprobe (1σ relative standard deviation of 5%). The fused glasses were analyzed by FTIR to confirm the absence of volatiles (see 2.3.2).

Gold−palladium (Au_{80}−Pd_{20}) tubes (40mm i.d. / 45mm o.d. / 10mm long) were used for the high−pressure experiments. Cut and annealed tubes were first triple−crimped, welded shut, and flattened at one end. They were then ultrasonically cleaned in dichloromethane for 30 minutes to remove any organic carbon present on the capsule surface (Mattey, 1991) and stored at 110°C for at least 24 hours prior to use. A total of 120mg of starting material, including H_2O and mixed carbon source, was loaded into pre−cleaned capsules. Dihydrated oxalic acid ($C_2H_2O_4 \cdot 2H_2O$; $\delta^{13}C = -26.7‰\pm0.2‰$) and a natural dolomite ($\delta^{13}C = 2.9‰\pm0.2‰$) were used as carbon sources. It is assumed that CO_2 adsorption on the carbon source or starting material was insignificant. The two carbon sources were mixed in different ratios to obtain the desired $\delta^{13}C$−value and CO_2 concentration, which were weighed on a microbalance (±0.001mg). 1wt% H_2O was added to ensure that the melt reached the liquidus (e.g., Médard and Grove, 2008). The other end of the filled capsules was then closed by triple crimping, welding, and flattening. The flattened final capsule was approximately 6mm in length (Fig. S1).

All experiments were conducted using a piston−cylinder apparatus at the Lamont−Doherty Earth Observatory (Columbia University) in New York, USA. Run conditions were set in such a way that the melt would be undersaturated with respect to volatiles and above the liquidus (1.5 GPa/1270°C and 1.0 GPa/1240°C for the MORB series and 1.5 GPa/1280°C and 1.0 GPa/1265°C for the Basanite series). After reaching the target P−T, the experiments were left for 2 hours without any attempt to control the oxygen fugacity. It was then quenched by turning off the electrical power. It took about 5 seconds to cool to less than 400°C. The pressure decreased during the quenching, however, the resulting glass was observed to be vesicle−free under the microscope. The filled Au_{80}−Pd_{20} capsule was centered in a 35mm long cylindrical graphite furnace surrounded by a 6mm length high−density Al_2O_3 sleeve. MgO was used as a spacer to fill the other parts of the graphite furnace. The pressure medium outside of the graphite furnace was 35mm long cylindrical Pb−wrapped CaF_2. A D−type ($W_{97}Re_3$–$W_{75}Re_{25}$) thermocouple located ~1mm from the capsule, separated by a 1mm thick Al_2O_3 wafer, provided accurate temperature readings during the run. The assembly diagram is shown in Figure S1.

2.3. Characterization

2.3.1. $\delta^{13}C$−value analysis by EA−IRMS

The $\delta^{13}C$ values of the synthetic glasses were determined using a Costech elemental analyzer (ECS4010) coupled to a ConFlo IV and Thermo Scientific Delta V plus Isotope Ratio Mass Spectrometer (EA−IRMS) at the Lamont−Doherty Earth Observatory, Columbia University, New York, USA. Prior to analysis, the glasses were carefully picked by hand under a stereomicroscope and then ultrasonically cleaned with dichloromethane for 30 minutes to ensure the removal of any organic contaminants. After cleaning, the samples were dried at 110°C for a minimum of 24 hours. Accurate amounts of each glass were weighed on a microbalance (±0.001mg) (Table S1), encapsulated in 3.2×4mm tin capsules, and stored in a desiccator until analysis.

The encapsulated samples were combusted at ~1700°C, over a chromium (III) oxide catalyst in the presence of excess oxygen (25ml/min). Helium was used as a carrier gas at a rate of 100ml/min. A silvered cobalt/cobalt oxide, placed in the quartz combustion tube, ensured the complete conversion of sample carbon to CO_2 and the removal of residual halogens or sulfur. The CO_2 peaks for each sample were then separated on a gas chromatography (GC) column (operating at 55°C) prior to analysis by IRMS.

The $\delta^{13}C$−values obtained for each sample were calibrated using a three−point regression method against the standards USGS24 (graphite; $\delta^{13}C = -16.05\pm0.07$‰, V−PDB; United States Geological Survey Reston Stable Isotope Laboratory, 2019a), USGS40 (L−glutamic acid; $\delta^{13}C = -26.39\pm0.04$‰, V−PDB, United States Geological Survey Reston Stable Isotope Laboratory, 2019b), and USGS41 (L−glutamic acid; $\delta^{13}C = 37.63\pm0.05$‰, V−PDB; United States Geological Survey Reston Stable Isotope Laboratory, 2011). The average analytical internal error of the $\delta^{13}C$−value, calculated to be ±0.2‰, was determined based on standard deviation (1σ) of repeated EA−IRMS measurements of the carbon source, oxalic acid. Craig correction is applied to account for the oxygen isotope effect (Craig, 1957). To ensure instrument performance and monitor drift, one set of standards was analyzed for every ~10 samples.

2.3.2. H_2O and CO_2 concentration analysis by FTIR

H_2O and CO_2 concentrations in the synthetic glasses were determined using a Thermo Nicolet iN10 Fourier Transform Infrared (FTIR) spectrometer at Lamont−Doherty Earth Observatory. The instrument was purged with dry, CO_2−scrubbed air, and measurements were facilitated by a liquid nitrogen−cooled MCT−A detector. Preparation of the glass chips involved double polishing with alumina−coated paper. Chip thicknesses ranged from 15 to 100μm. Prior to measurement, the chips were washed with acetone to remove residual crystal bond. Thickness was determined by the reflectance method (±3μm; Nichols and Wysoczanski, 2007).

Spectra were acquired in the range of 400−8000cm^{-1} with 256 scans and a resolution of 1cm^{-1} in transmitted mode. The aperture size was set to 100μm for both width and height. Each sample was analyzed on 2 to 8 spots to ensure homogeneity of H_2O and CO_2 content (Table S2). The error is estimated by the standard deviation (1σ) of measurements at different points. Total water content was determined from the intensity of the OH^- stretching band at approximately 3550cm^{-1}, while CO_2 concentration was derived from the doublet peak at 1515cm^{-1} and 1435cm^{-1}. Peak heights were determined by subtracting from the target spectra the volatile−free glass whose composition matches the target spectra. The absorption coefficients for CO_2 and H_2O were selected from Shishkina et al. (2014) based on their closest match to the composition of the target glass. The effects of H_2O and CO_2 have been taken into account when calculating glass density (Bourgue and Richet, 2001; Lesher and Spera, 2015).

2.3.3. Major element composition analysis by electron microprobe

The major element compositions of the glasses were determined using a Cameca SX5−Tactis electron microprobe at the American Museum of Natural History (AMNH). An acceleration voltage of 15kV and a defocused beam of 10μm were used. Beam currents varied depending on the element, ranging from 4nA for Na (with a 10 s count time) to 10nA for others (with 20 s count times). Na analysis was done first to minimize potential Na migration. Background count times were set to half of peak count times. The instrument was calibrated using natural and synthetic mineral standards deposited at AMNH, including potassium feldspar (Al, Si, and K), rutile (Ti), fayalite (Fe), rhodonite (Mn), olivine (Mg), anorthite (Ca), jadeite (Na), and apatite (P). Major element compositions were obtained by averaging 10 random spots on the glass, and errors were estimated from the standard deviation of the 10 replicate analyses.

2.4. Ion microprobe methods

2.4.1. Sample preparation for SIMS

The background levels in the ion microprobe sample chamber for CO_2 and $\delta^{13}C$−value measurements determine the vacuum quality. To reduce the background interference from carbon, the reference materials were pressed into indium metal (>99.9% purity). The samples were prepared with crystal bond and single−side hand polished down to 0.3μm using corundum mats and alumina grit. The crystal bond was then removed with acetone and soaked for several hours. The samples were then embedded in indium metal and pressed overnight to achieve a flat surface.

Two 25.5mm diameter twin mounts, with a central 17mm part filled with indium, were prepared with pieces of the same glass shards for the analysis sessions at Nancy and WHOI, respectively (Fig. S2). The final sample mount surface was cleaned with deionized and Millipore filtered water, dried, and then coated with a ~20nm gold layer to ensure surface conductivity.

2.4.2. Secondary Ion Mass Spectrometry at CRPG–CNRS–Nancy (2023 December)

Analyses were performed on a CAMECA IMS 1270 E7 ion microprobe at CRPG−CNRS−Nancy, France in December 2023. Before analysis, the mount is left in the airlock of the SIMS for 24 hours prior to the analytical session to reach vacuum conditions $< 6\times10^{-9}$ Torr. A Cs^+ primary beam was accelerated using a potential of 10kV. To maintain optimal signal levels for all reference materials, the primary intensity was adjusted in the range of 0.2 to 3.6nA for the detector to receive a signal of ^{12}C within the range of 200,000 to 300,000 counts per second (cps). Average ion yields throughout the session were 68 cps/ppm/nA for ^{12}C and 0.7 cps/ppm/nA for ^{13}C. The normal electron gun was used to compensate for Cs^+ ions charges on the sample surface.

Secondary negative ^{12}C and ^{13}C ions were detected with an axial electron multiplier (EM) using a magnetic peak switching technique in mono−collection mode, since the axial EM is more resistant to aging than off−axis EMs. Also, the mono−collection setup was chosen to mitigate differential detector aging between ^{12}C and ^{13}C due to the much higher count rate of ^{12}C compared to ^{13}C. ^{18}O was measured on FC2, the axial Faraday Cup (FC) equipped with a 10^{12} Ohm resistor. The ^{12}C signal was tried to maintain < 300,000 cps to mitigate aging of the EM. Background measurements for the axial EM and FC2 were performed at mass 11.8 and mass 17.8, respectively. The mass resolving power (MRP) was set to 5000, which is sufficient for resolving ^{13}C from $^{12}C^{1}H$, but not so high to unnecessarily cut out the ^{13}C signal. Analysis parameters included a field aperture size of 2500μm, entrance slit of 100μm, exit slit of 243μm, contrast aperture of 400μm, PBMF aperture of 3000μm and L4 aperture of 750μm. The energy slit was centered, shifted by 5eV and opened to 30eV.

A 120 second pre−sputtering was performed using a $15\times15\mu m^2$ square raster to reduce surface contamination, minimize background counts, and remove the gold layer, followed by analyses on a $10\times10\mu m^2$ rastered spot positioned at the center of the gridded clean area. Automatic centering of the transfer deflectors and mass was implemented in the analysis routine. Counting times were set to 4 seconds for EM background, 4 seconds for ^{12}C, 20 seconds for ^{13}C, 4 seconds for FC background, and 2 seconds for ^{18}O. Waiting times between mass measurements were set to 3, 1, 1, 1, and 1 second, respectively. A 89 nanoseconds deadtime for the EM has been determined at the beginning of the analytical session. Each measurement consisted of 30 cycles, resulting in an average analysis time of approximately 30 minutes. Further discussion of precision, accuracy, and drift can be found in the results section.

2.4.3. Secondary Ion Mass Spectrometry at Woods Hole Oceanographic Institution (2024 March)

Analyses were performed on a CAMECA IMS 1280 ion microprobe at the Northeast National Ion Microprobe Facility at the Woods Hole Oceanographic Institution (WHOI). Before measurements, the mount was outgassed for about an hour in an airlock until the pressure reached below 5×10^{-8} Torr. Further outgassing occurred upon insertion into the sample chamber, and analyses began only after the sample chamber pressure reached below 5×10^{-9} Torr. The $^{133}Cs^{+}$ primary beam was accelerated at a potential of 10kV. The beam current was adjusted within a range of 0.6 to 4.6nA, depending on the expected CO_2 concentration in each glass, to obtain 300,000 cps of ^{12}C and 3,000 cps of ^{13}C. This adjustment was made to achieve count rates on ^{12}C and ^{13}C that enabled $^{13}C/^{12}C$ measurement precision at or below 1.0 ‰ (standard error of the mean) for most glasses.

The electron gun (e−gun) was tuned using a standard protocol developed for all measurements using a $^{133}Cs^{+}$ beam. The e−gun filament was set for a current of ~1.5mA at full emission, and with a final emission current of ~0.2mA with wehnelt set to −140V. After tuning of the primary beam and centering of the $^{27}Al^{16}O^{-}$ secondary beam in the center of the Cu−Al grid, final tuning of the e−gun was guided by channel plate imaging of $^{1}H^{-}$ ions produced by the e−gun e^{-} cloud interacting with the sample surface. To optimize the e−gun tuning, deflectors (D1 and D2), quad e^{-}, ion coil, and lens (Le^{-}, ~7500V) settings were tuned to maximize the sample current with an energy offset of 20ev. With e^{-} on, the secondary $^{1}H^{-}$ channel plate image was used for final tuning of the e−gun cloud, producing a symmetrical (round) and homogeneous $^{1}H^{-}$ image. Bxe− and Bye− coils were adjusted to center the $^{1}H^{-}$ image from the e− beam with the $^{1}H^{-}$ image produced by the $^{133}Cs^{+}$ ion beam. The energy offset was removed such that equal high voltages of ~10kV were obtained between the sample and e−gun, and the sample current was between 0 and 1µA.

Secondary ions were counted in multi−collector mode, with different secondary magnet settings and detectors for measuring secondary ions of carbon masses and oxygen reference mass, respectively, within each measurement cycle. ^{12}C and ^{13}C were counted simultaneously using EMs at trolley positions L2 for ^{12}C (deadtime = 63.1 nS) and H2 for ^{13}C (deadtime = 63.7 nS) with the secondary magnet set for axial mass 12.5. A high voltage adjustment was made on the electron multiplier at L2 before each measurement to mitigate the effects of detector aging due to the high ^{12}C signal. ^{18}O was measured on a Faraday Detector with 10^{11} Ohm resistor at trolley position H2, with the magnet set for axial mass 17.9. A 250μm−wide slit was placed in front of each detector to achieve a mass resolving power of ~5000. Analyses consisted of 30 cycles with count times of 2 seconds for ^{18}O and 20 seconds for ^{12}C and ^{13}C.

For the first three sessions, the focused primary bean was rastered over an area of 15×15μm^2 and pre−sputtered for 120 seconds, then the raster was reduced to 10×10μm^2 during the measurement. Analysis crater diameter ranged from ~15 to just over 20μm, depending on the primary beam current used. The field aperture of 3000μm, contrast aperture of 400μm diameter, and an entrance slit of 200μm width were applied to the secondary ions. Measurement of CO_2 in the olivine crystals (considered as a background level) yielded ^{12}C and ^{13}C signals that were < 10% of the total ^{12}C and ^{13}C signals measured on most of the glasses, but > 10% in lower CO_2 concentration glasses (Table S3). Average ion yields for the first three sessions were 65 cps/ppm/nA for ^{12}C and 0.7 cps/ppm/nA for ^{13}C, which is comparable to the session in Nancy.

For the last two sessions days, the analytical procedure was modified to minimize the incorporation of surface and background carbon into the measurements. Although the same primary beam currents were used, the pre−sputter time was increased to 300 seconds and the raster during the pre−sputter was increased to 20×20μm^2. The secondary field aperture size was decreased to 1500μm in order to block the transmission of surface ions from the center of the sputtering crater. With the increased pre−sputter time and decreased field aperture size, the carbon background contribution, as measured on presumed carbon−free olivine crystals on the mount, was <1 % of the total signal measured on most glasses in the session (3−6% for DR52 – 380 ppm CO_2) (Table S3). Average ion yields decreased for the last two sessions, 36 cps/ppm/nA for ^{12}C and 0.4 cps/ppm/nA for ^{13}C. The total analysis time per spot was approximately 15 minutes. Five spots were measured on each glass shard. Any precision, accuracy, and drift will be further discussed in the results section.

3. Results

3.1. Characterization of the reference materials

3.1.1. Glass appearance

For the MORB and Basanite series, approximately 120mg of material was fused for each sample (see 2.2). The resulting glass recovered from the capsules was olive green or greenish brown. The color was generally uniform. No bubbles were observed within the glass at 500x magnification. In addition, quench crystals were absent from both microscope at 500x magnification and SEM images (Fig. S3). The NBO, Etna, and Hawaii samples are also quench crystal free glasses described in detail in Lee et al. (2024). DR52 consists of 5% microphenocrysts of plagioclase and olivine and 95% glass. The microphenocrysts were avoided in the analysis and only the glass was analyzed.

3.1.2. Major element composition

All major element compositions and standard deviations on 10 repeat analyses are provided in Table 1 and Fig. 1 for all the MORB and Basanite series and test glasses. In all cases the glass composition was found to be homogeneous with a relative standard deviation (RSD) of less than 5% on most element abundance.

Table 1

Major element (in wt.%) measured by electron microprobe and volatile (CO_2 in ppm and H_2O in wt.%) composition measured by FTIR (See 2.3). $\delta^{13}C$—values are determined by EA—IRMS. Standard deviation (1σ) of each measurement is provided in parentheses.

Name	Type	CO_2	$\delta^{13}C$	H_2O	SiO_2	TiO_2	Al_2O_3	FeO	MnO	MgO	CaO	Na_2O	K_2O	P_2O_5	Total
CI_Ref_4	MORB[1]	9200	-26.4	1.2	48.3	1.4	17.4	10.5	0.2	7.3	11.3	2.6	0.1	0.2	99.3
		(500)	(0.2)	(0.1)	(0.4)	(0.1)	(1.1)	(0.5)	(0.0)	(0.1)	(0.3)	(0.1)	(0.0)	(0.0)	(0.3)
CI_Ref_6	MORB[1]	5100	-26.2	1.1	49.7	1.4	16.0	10.7	0.2	7.1	11.6	2.6	0.2	0.1	99.7
		(200)	(0.2)	(0.1)	(0.3)	(0.1)	(0.1)	(0.1)	(0.0)	(0.1)	(0.1)	(0.1)	(0.0)	(0.0)	(0.4)
CI_Ref_9	MORB[1]	8000	-6.9	1.6	49.0	1.4	15.8	10.6	0.2	7.2	11.6	2.6	0.2	0.1	98.7
		(300)	(0.3)	(0.1)	(0.2)	(0.1)	(0.1)	(0.1)	(0.0)	(0.1)	(0.1)	(0.1)	(0.0)	(0.0)	(0.4)
CI_Ref_10	MORB[1]	5800	-13.8	0.8	48.6	1.4	15.8	10.8	0.2	7.1	12.4	2.6	0.2	0.1	99.1
		(1000)	(0.6)	(0.1)	(0.5)	(0.1)	(0.1)	(0.2)	(0.0)	(0.1)	(0.4)	(0.2)	(0.0)	(0.0)	(0.6)
CI_Ref_11	MORB[1]	7000	-27.4	1.1	49.2	1.4	15.8	11.0	0.2	7.0	11.4	2.5	0.2	0.1	98.8
		(500)	(0.2)	(0.2)	(0.1)	(0.1)	(0.1)	(0.1)	(0.0)	(0.1)	(0.1)	(0.2)	(0.0)	(0.0)	(0.2)

CI_Ref_15	MORB[1]	2300	-7.9	1.0	49.4	1.4	15.9	10.9	0.2	7.2	11.6	2.6	0.2	0.1	99.5
		(300)	(0.2)	(0.1)	(0.2)	(0.1)	(0.1)	(0.2)	(0.0)	(0.1)	(0.1)	(0.2)	(0.0)	(0.0)	(0.3)
CI_Ref_18	MORB[1]	2700	-24.3	1.1	49.5	1.4	16.0	11.1	0.2	7.1	11.5	2.6	0.2	0.1	99.6
		(400)	(0.2)	(0.1)	(0.2)	(0.1)	(0.1)	(0.1)	(0.0)	(0.1)	(0.1)	(0.1)	(0.0)	(0.0)	(0.3)
CI_Ref_20	MORB[1]	2800	-23.1	0.8	49.8	1.3	16.0	11.1	0.2	7.1	11.5	2.5	0.2	0.1	99.9
		(300)	(0.2)	(0.1)	(0.2)	(0.1)	(0.1)	(0.2)	(0.0)	(0.1)	(0.1)	(0.1)	(0.0)	(0.0)	(0.4)
CI_Ref_22	MORB[1]	2100	-21.7	0.9	49.5	1.4	15.9	11.0	0.2	7.2	11.6	2.6	0.2	0.1	99.7
		(100)	(0.2)	(0.1)	(0.3)	(0.1)	(0.1)	(0.1)	(0.0)	(0.1)	(0.1)	(0.1)	(0.0)	(0.0)	(0.4)
CI_Ref_23	MORB[1]	2700	-27.7	1.2	49.6	1.4	15.9	11.0	0.2	7.1	11.4	2.6	0.2	0.1	99.6
		(400)	(0.2)	(0.1)	(0.2)	(0.1)	(0.1)	(0.2)	(0.0)	(0.1)	(0.2)	(0.1)	(0.0)	(0.0)	(0.3)
CI_Ref_25	MORB[1]	9000	-9.9	1.0	48.9	1.4	15.8	11.0	0.2	7.1	12.2	2.5	0.2	0.1	99.4
		(1300)	(0.2)	(0.1)	(0.3)	(0.1)	(0.1)	(0.1)	(0.0)	(0.1)	(0.2)	(0.2)	(0.0)	(0.0)	(0.3)
CI_Ref_27	MORB[1]	5300	-27.6	1.2	49.5	1.4	15.7	11.0	0.2	7.1	11.5	2.5	0.2	0.1	99.1
		(800)	(0.2)	(0.2)	(0.3)	(0.1)	(0.2)	(0.1)	(0.0)	(0.1)	(0.1)	(0.1)	(0.0)	(0.0)	(0.3)
CI_Ref_28	MORB[1]	8900	-27.3	1.4	49.1	1.3	15.8	11.0	0.2	7.1	11.4	2.6	0.2	0.1	98.8
		(900)	(0.2)	(0.1)	(0.2)	(0.1)	(0.2)	(0.2)	(0.0)	(0.1)	(0.1)	(0.1)	(0.0)	(0.0)	(0.3)
CI_bas_1	Basanite[1]	12000	-26.8	1.7	44.5	4.3	15.0	12.3	0.2	5.3	9.9	4.2	1.7	1.0	98.3
		(700)	(0.3)	(0.2)	(0.3)	(0.1)	(0.1)	(0.2)	(0.0)	(0.1)	(0.1)	(0.1)	(0.1)	(0.1)	(0.3)
CI_bas_2	Basanite[1]	3600	-25.6	1.7	44.8	4.3	15.0	12.4	0.2	5.4	9.9	4.1	1.7	1.0	98.7
		(400)	(0.2)	(0.2)	(0.2)	(0.1)	(0.1)	(0.2)	(0.0)	(0.1)	(0.1)	(0.1)	(0.1)	(0.1)	(0.3)
CI_bas_3	Basanite[1]	5800	-1.1	1.5	44.5	4.2	15.0	12.0	0.2	5.5	10.2	4.1	1.8	0.9	98.4
		(800)	(0.2)	(0.2)	(0.5)	(0.1)	(0.3)	(0.1)	(0.0)	(0.1)	(0.3)	(0.2)	(0.1)	(0.1)	(0.5)
CI_bas_4	Basanite[1]	2200	-11.9	1.3	44.5	4.3	14.9	12.5	0.2	5.4	10.5	4.2	1.7	0.9	99.0
		(500)	(0.2)	(0.2)	(0.8)	(0.1)	(0.3)	(0.2)	(0.0)	(0.1)	(0.4)	(0.2)	(0.1)	(0.1)	(0.6)
CI_bas_5	Basanite[1]	1800	-8.6	1.6	44.7	4.2	15.0	12.3	0.2	5.3	10.3	4.1	1.8	1.0	98.8
		(200)	(0.2)	(0.1)	(0.5)	(0.1)	(0.2)	(0.2)	(0.0)	(0.1)	(0.3)	(0.2)	(0.1)	(0.1)	(0.5)
CI_bas_6	Basanite[1]	8400	-26.0	1.7	44.9	4.2	15.0	12.3	0.2	5.3	9.8	4.2	1.7	1.0	98.6
		(800)	(0.2)	(0.1)	(0.3)	(0.1)	(0.1)	(0.1)	(0.0)	(0.1)	(0.1)	(0.1)	(0.1)	(0.1)	(0.4)
CI_bas_7	Basanite[1]	3600	-14.5	1.3	44.4	4.3	14.9	12.4	0.2	5.4	10.4	4.2	1.7	1.0	98.8
		(500)	(0.2)	(0.1)	(0.8)	(0.1)	(0.2)	(0.3)	(0.0)	(0.1)	(0.4)	(0.2)	(0.1)	(0.1)	(0.9)
CI_bas_8	Basanite[1]	4100	-9.1	1.3	43.9	4.3	14.7	12.2	0.2	5.3	11.0	4.1	1.7	1.0	98.3
		(600)	(0.6)	(0.2)	(0.7)	(0.1)	(0.3)	(0.1)	(0.0)	(0.1)	(0.3)	(0.2)	(0.1)	(0.1)	(0.6)
CI_bas_9	Basanite[1]	7600	-13.0	1.1	44.0	4.3	14.7	12.6	0.2	5.4	10.5	4.2	1.7	1.0	98.6
		(900)	(0.2)	(0.3)	(0.5)	(0.1)	(0.2)	(0.1)	(0.0)	(0.1)	(0.3)	(0.2)	(0.1)	(0.1)	(0.6)
CI_AMNH_NBO_1_3	NBO[2]	800	-27.3	2.5	56.4	2.7	18.4	6.7	0.1	3.4	6.0	2.4	1.0	0.6	97.7
		(200)	(0.2)	(0.5)	(0.6)	(0.1)	(0.4)	(0.2)	(0.0)	(0.1)	(0.1)	(0.1)	(0.1)	(0.0)	(0.3)
CI_AMNH_NBO_2	NBO[2]	1000	-27.5	2.9	54.7	3.0	16.5	7.8	0.1	3.7	6.7	2.9	1.3	0.7	97.4
		(200)	(0.2)	(0.4)	(0.2)	(0.1)	(0.1)	(0.2)	(0.0)	(0.1)	(0.1)	(0.1)	(0.1)	(0.1)	(0.4)
CI_AMNH_NBO_3_1	NBO[2]	1400	-27.7	2.7	49.7	3.5	17.2	9.0	0.2	4.4	7.9	3.2	1.4	0.8	97.2
		(100)	(0.2)	(0.3)	(0.3)	(0.1)	(0.1)	(0.1)	(0.0)	(0.1)	(0.1)	(0.1)	(0.1)	(0.1)	(0.6)

CI_AMNH_NBO_4	NBO[2]	1900	-27.0	2.3	47.7	3.9	15.7	10.2	0.2	4.8	8.7	3.6	1.6	0.8	97.2
		(400)	(0.2)	(0.2)	(0.3)	(0.1)	(0.1)	(0.1)	(0.0)	(0.1)	(0.1)	(0.1)	(0.1)	(0.1)	(0.4)
DR52	Test	380[4]	-8.2[4]	0.0[4]	50.3	1.4	16.7	10	0.2	8.9	11.1	3.0	0.1	0.1	101.8
	(DR52[3])_	(40)	(0.2)	(0.0)	(0.3)	(0.1)	(0.1)	(0.1)	(0.0)	(0.1)	(0.1)	(0.1)	(0.0)	(0.0)	(0.5)
ETNA3−2	Test	3300	-22.7	2.7	47.9	1.6	16.3	9.7	0.2	6.3	10.5	3.2	1.9	0.5	98.1
	(ETNA[2])	(200)	(0.2)	(0.1)	(0.2)	(0.1)	(0.1)	(0.1)	(0.0)	(0.1)	(0.1)	(0.2)	(0.1)	(0.0)	(0.4)
ETNA3−2bis	Test	3300	-22.2	2.8	47.8	1.6	16	10.4	0.2	6.2	10.3	3.2	1.8	0.5	98.1
	(ETNA[2])	(100)	(0.2)	(0.1)	(0.2)	(0.1)	(0.1)	(0.1)	(0.0)	(0.1)	(0.1)	(0.1)	(0.1)	(0.0)	(0.3)
ETNA3−3	Test	3600	-24.2	1.7	48.9	1.6	16.2	9.8	0.2	6.3	10.6	3.3	1.9	0.6	99.3
	(ETNA[2])	(300)	(0.2)	(0.1)	(0.6)	(0.1)	(0.2)	(0.3)	(0.0)	(0.1)	(0.1)	(0.1)	(0.1)	(0.0)	(0.3)
CI_IPGP_B6	Test	1900	-28.1	1.5	49.5	2.1	11.6	12	0.2	11.8	9.8	1.9	0.4	0.2	99.5
	(Hawaii[2])	(500)	(0.2)	(0.1)	(0.2)	(0.1)	(0.2)	(0.1)	(0.0)	(0.3)	(0.1)	(0.1)	(0.1)	(0.0)	(0.3)

[1] This study

[2] Lee et al. (2024)

[3] Maevaray, (2017)

[4] Measured by step−heating method

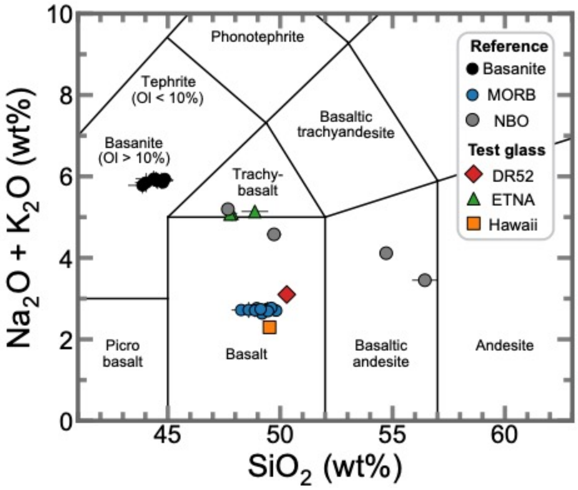

Fig. 1 Total alkali versus silica diagram showing the composition of the reference materials including test glasses.

3.1.3. Volatile concentrations

Reference materials including test glasses range in CO_2 concentrations from 380±40 to 12000±700 ppm (Fig. 2 and Table 1). The CO_2 concentrations of the MORB series range from 2000±100 to 9200±400 ppm, while the Basanite series has a wider range, covering values from 1800±200 to 12000±700 ppm. The range of H_2O concentrations is relatively limited, with average values of 1.3wt% including both the MORB and Basanite series, ranging from 0.8±0.1 to 1.7±0.1wt%. The NBO series has a lower range of CO_2 concentration than MORB and Basanite, ranging from 800±100 to 1900±300 ppm. H_2O content of NBO series is higher than the

MORB and Basanite, ranging from 2.3±0.1 to 2.9±0.4wt%. The errors in CO_2 and H_2O measurements were estimated as the standard deviation (1σ) of 3 to 9 repeated FTIR analyses, as shown in Table 1.

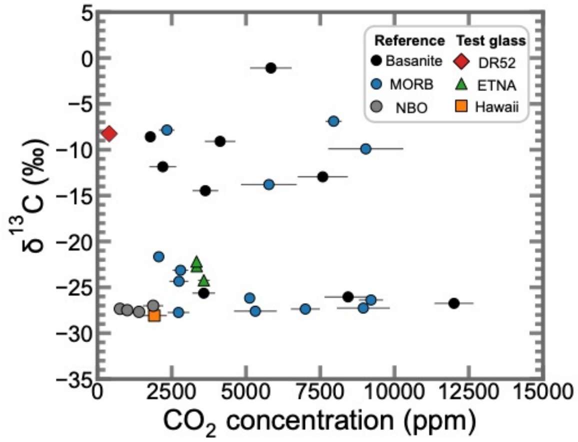

Fig. 2 $\delta^{13}C$–value versus CO_2 content of series of reference materials and test glasses. X–axis shows CO_2 concentration measured by FTIR. The error bar represents the standard deviation on 3 to 9 repeated analyses. Y–axis shows the $\delta^{13}C$–value measured by EA–IRMS and the error bar represents either the analytical error (0.2‰) or the standard deviation on repeated analysis (see 3.1.3 for details) but are all smaller than the symbols.

3.1.4. $\delta^{13}C$–value by EA−IRMS

The $\delta^{13}C$–values of the reference materials range from –1.1±0.2 to –28.1±0.2‰ (Fig. 2 and Table 1). The MORB series, $\delta^{13}C$–values range from –6.9±0.3‰ to –27.7±0.2‰, and the Basanite series from –1.1±0.2‰ to –26.8±0.2‰. The NBO series is characterized by a more limited range of $\delta^{13}C$–values, ranging from –27.0±0.2‰ to –27.7±0.2‰. Due to the limited amount of sample and the destructive nature of the analyses only 10 reference materials were measured multiple times. For samples that were measured more than once, the error was assessed by calculating the standard deviation of the repeated measurements (1σ), which ranged from ±0.2‰ to ±0.6‰ (average ±0.2‰). Samples analyzed only once were assigned an error estimated from the analytical error of the EA–IRMS which is ±0.2‰. The error of the EA–IRMS was not correlated with the measured sample weight or CO_2 concentration. All EA–IRMS data and measured weight are available in Table S1.

3.2. $\delta^{13}C$–value analysis by SIMS

Data from SIMS measurements at Nancy and WHOI are available in Tables S4–S7.

3.2.1. Precision and homogeneity

The internal precision for δ^{13}C–value measurements performed by SIMS including both series of reference materials and test glasses, represented by the standard error of the mean (1σ) of each analysis, ranged from ±0.5 to ±1.9‰ (avg. ±0.7‰) on the Nancy IMS 1270 and from ±0.6 to ±1.7‰ (avg. ±1.1‰) on the WHOI IMS 1280. Notably, the internal precision improved significantly with increasing ^{12}C and ^{13}C counts (Fig. 3). Beyond 200,000 cps on ^{12}C and 2,000 cps on ^{13}C, the internal precision mostly improved to less than ±1.0‰ for both instruments. The result with a total count of 1,200,000 for ^{13}C (calculated as 2,000 cps × 20 seconds × 30 cycles) aligns well with the statistical expectation. A SIMS analysis with a total count of 10^6 of a rare isotope (^{13}C in this case) is expected to have a theoretical precision of 1‰ in the isotope ratio (e.g., Fitzsimons et al., 2000; Valley and Graham, 1991). Internal precision levels for comparable carbon counts remained similar before and after the change in analytical parameters at the WHOI sub–sessions (see 2.4.3). Thus, optimization of primary beam intensity and analytical conditions to maximize ^{12}C and ^{13}C counts is critical to achieve high internal precision.

External precision, also called reproducibility or repeatability, is represented by the standard deviation on repeated analyses. The external precision was calculated from the standard deviation (1σ) of the instrumental mass fractionation (IMF) corrected δ^{13}C–value (see 3.2.3 for detailed correction). In both the WHOI and Nancy instruments, the average reproducibility of δ^{13}C–value was ±0.9‰ for Nancy (ranging from ±0.4 to ±2.4‰) and ±1.0‰ for WHOI (ranging from ±0.3 to ±2.7‰) (Table 2). Average reproducibility on the WHOI instrument improved from ±1.3‰ (1st–3rd sub–sessions) to ±0.9‰ (4th and 5th sub–sessions) after decreasing the field aperture size and increasing the pre–sputter time, which may indicate a reduction in heterogeneous background contributions from spot to spot. In theory, the external precision and the average internal precision for a series of analyses of an isotopically homogeneous sample should be equivalent (e.g., Fitzsimons et al., 2000). The isotopic homogeneity of the reference materials was supported by the similarities of external and internal precision values (0.3‰ and 0.4‰ average difference for Nancy and WHOI, respectively; Table 2 and Fig. 4).

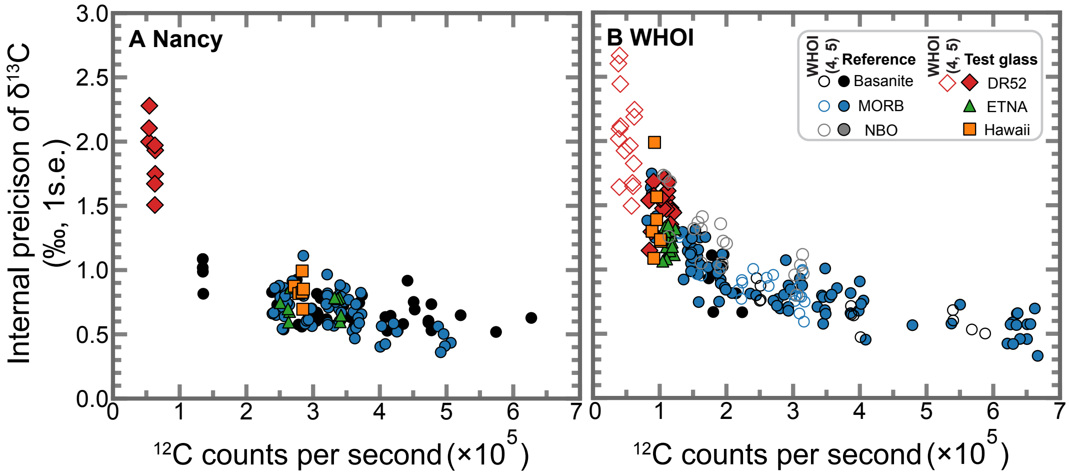

Fig. 3 Internal precision (1s.e., standard error of the mean) of the δ^{13}C–value (in ‰, V–PDB) versus counts per second (cps) of ^{12}C in the axial electron multiplier (EM). (A) and (B) show ^{12}C results obtained on the Ion Microprobe in Nancy and on the Ion Microprobe in WHOI, respectively. Closed symbols represent Nancy and 1st–3rd sub–sessions of WHOI. Open symbols represent 4th and 5th sub–sessions of WHOI. ^{13}C results show an almost identical pattern with a ratio of ~1/100. Both results show that the precision improves as the count rate of ^{12}C and ^{13}C increases. In particular, the precision is better than ±1.0‰ above 200,000 cps on ^{12}C and 2,000 cps on ^{13}C.

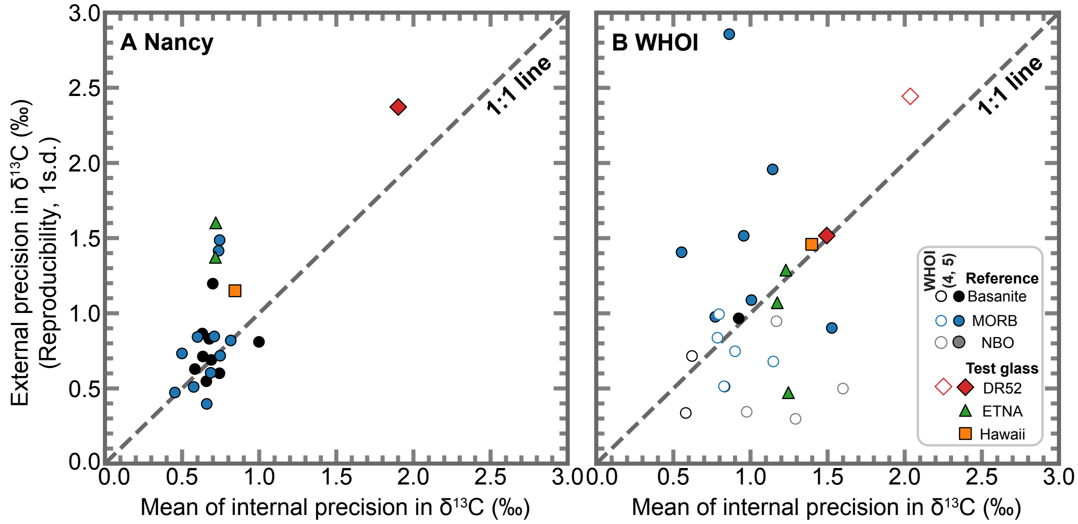

Fig. 4 Internal versus external precision (reproducibility) for the SIMS results obtained at (A) Nancy and (B) WHOI. The x–axis represents the average internal precision in δ^{13}C–values (‰, V–PDB) for repeated measurements on the same glass chips, while the y–axis represents the external precision, reproducibility, indicated by the standard deviation (1s.d.) of the IMF corrected δ^{13}C–values. Ideally, a homogeneous sample would have identical internal and external precision. The dashed line represents a 1:1 relationship. Closed symbols represent Nancy and the 1st to 3rd sub–sessions of WHOI, while open symbols represent the 4th and 5th sub–sessions of WHOI.

Table 2

Summary of internal precision (1σ) and external precision (reproducibility) (1σ) of $\delta^{13}C$ SIMS measurement from Nancy and WHOI in permil (‰, V−PDB)

Name	Type	Number of measurements	Internal precision	External precision	Number of measurements	Internal precision	External precision
			Nancy			WHOI	
CI_Ref_4	MORB				4*	0.8	0.5
CI_Ref_6	MORB	5	0.7	0.6	8	1.0	1.1
CI_Ref_9	MORB	5	0.6	0.5	4*	0.8	1.0
CI_Ref_10	MORB	5	0.7	0.7	8	0.8	1.0
CI_Ref_11	MORB	5	0.5	0.7	4*	0.8	0.9
CI_Ref_15	MORB	5	0.6	0.8	32	0.9	2.9
					5*	1.1	0.7
CI_Ref_18	MORB	5	0.7	1.5	8	1.0	1.5
CI_Ref_20	MORB	5	0.7	0.8			
CI_Ref_22	MORB	5	0.8	0.8	8	1.1	2.0
CI_Ref_23	MORB	6	0.8	0.8	7	1.5	0.9
CI_Ref_25	MORB	5	0.5	0.5			
CI_Ref_27	MORB	5	0.7	0.4	16	0.6	1.4
					8*	0.9	0.8
CI_Ref_28	MORB	5	0.7	1.4			
CI_bas_1	Basanite	5	0.7	0.5	4*	0.6	0.7
CI_bas_2	Basanite	5	0.7	0.8	9	0.9	1.0
CI_bas_3	Basanite	5	0.7	0.6	4*	0.6	0.3
CI_bas_4	Basanite	5	0.6	0.7			
CI_bas_5	Basanite	5	0.7	1.2			
CI_bas_6	Basanite	5	1.0	0.8	4*	0.8	0.5
CI_bas_7	Basanite	5	0.7	0.7			
CI_bas_8	Basanite	5	0.6	0.6			
CI_bas_9	Basanite	5	0.6	0.9			
CI_AMNH_NBO_1_3	NBO				4*	1.6	
CI_AMNH_NBO_2	NBO				5*	1.3	
CI_AMNH_NBO_3_1	NBO				5*	1.2	
CI_AMNH_NBO_4	NBO				5*	1.0	
DR52	Test (DR52)	8	1.9	2.4	18	1.5	1.5
					15*	2.0	2.5

ETNA3-2	Test (ETNA)	5	0.7	1.4	5	1.2	1.1
ETNA3-2bis	Test (ETNA)				3	1.2	0.5
ETNA3-3	Test (ETNA)	5	0.7	1.6	8	1.2	1.3
CI_IPGP_B6	Test (Hawaii)	6	0.8	1.1	7	1.4	1.5

* Marked are measured in 4th and 5th sub−sessions in WHOI.

3.2.2. IMF and drift

To ensure accurate results, it is imperative to calibrate the instrumental mass fractionation (IMF) and address any potential drift. IMF can be expressed in either α or δ notation, as described by eq.1 and eq.2, when R = $^{13}C/^{12}C$, $R_{measured}$ is the raw ratio measured by SIMS, and R_{true} is what we measured from EA−IRMS.

$$\mathrm{IMF}\ (\alpha) = \frac{R_{\mathrm{measured}}}{R_{\mathrm{true}}} \qquad \text{eq. 1}$$

$$\mathrm{IMF}\ (‰) = \left(\frac{R_{\mathrm{measured}}}{R_{\mathrm{true}}} - 1\right) \times 1000 \qquad \text{eq. 2}$$

IMF is due to the preferential ionization of lighter isotopes relative to heavier ones during secondary ion emission processes (e.g., Slodzian et al., 1980) as well as the differential transmission or detection of different isotopes (e.g., Sangely et al., 2014). This results in a depletion of the measured SIMS isotope ratios for heavier isotopes compared to the true ratio (e.g., De Hoog and EIMF, 2018; Hartley et al., 2012; Hauri et al., 2006). The extent of depletion depends on a number of factors, including instrument type, sample location, temporal drift, analytical configuration, primary beam intensity, and matrix composition effects.

Significant differences in IMF were observed between different facilities and setups at Nancy (ranges from α =0.955 to 0.971, avg. 0.963) and WHOI (ranges from α =0.968 to 0.989, avg. 0.980). We divided the WHOI session into five sub−sessions where different analysis conditions were used (Fig. 5). In the second session at WHOI, the mount was rotated 90 degrees and reinserted, and there was no systematic variation in IMF before and after reinsertion. In the third session at WHOI, the mount was reinserted, and a drift in IMF over time was characterized. However, in the fifth session at WHOI, DR52 analysis was inserted every 5 measurements, which showed no systematic drift over time. In the fourth and fifth sessions at WHOI, different analysis parameters from the first three sessions were attempted to reduce the background. The background was reduced by a factor of 10 by increasing the pre–sputter grid size from 15 µm to 20 µm, increasing the pre–sputter time from 120 to 300 seconds, and reducing the field aperture (from 3000 µm to 1500 µm) and exit slit (from 303 µm to 243 µm). This changes in analytical conditions resulted in a shift of the average IMF of 3‰.

A negative correlation between IMF and primary beam intensity (in the range of 0.2–2.2nA) was observed only in the Basanite series analyzed at Nancy (Fig. 6A). A linear regression calibration between beam intensity and IMF was performed to account for this variability. In the MORB series at Nancy (in the range of 0.5–2.4nA) (Fig. 6B) and in all series at WHOI, no such correlation was observed (Fig. S4). The effect of matrix composition on the IMF is discussed further in Section 4.5.

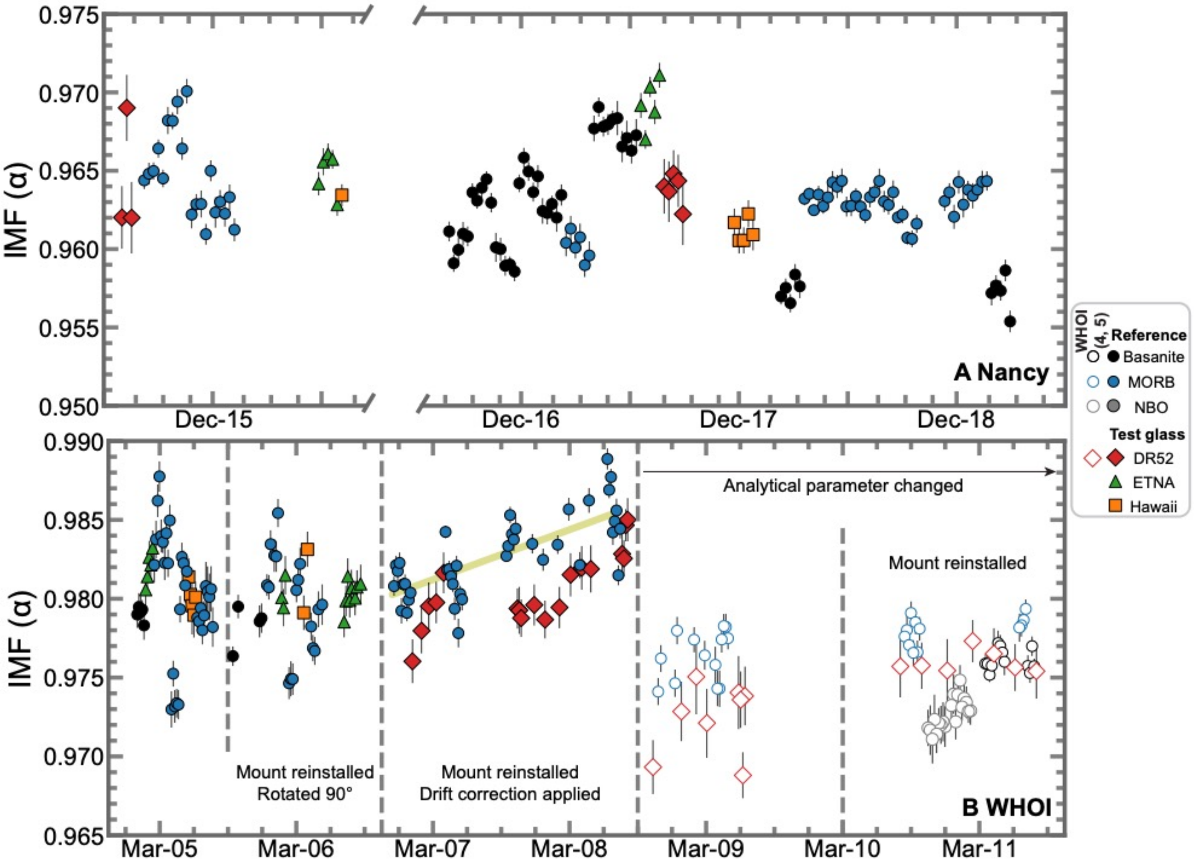

Fig. 5 Estimated IMF (in alpha) between carbon isotope ratio ($R={}^{13}C/{}^{12}C$) $R_{measured}$ measured by SIMS and R_{true} measured by EA–IRMS as a function of time during the (A) Nancy and (B) WHOI session. For Nancy, the x–axis is broken where there is no data. For WHOI session, the dashed line separates each sub–session, from the first to the fifth. From the first to the second sub–session the mount was reinstalled with a 90–degree rotation, resulting in IMF values comparable to the first sub–session. In the third sub–session, a drift over time was observed after

the mount reinstallation, with the green line representing a linear regression of the MORB reference materials used to track the drift. IMF changes occurred from the fourth sub−session due to changes in analytical parameters (see 3.2.2 for details). In the fifth sub−session, DR52 was analyzed every 5 measurements and showed no systematic drift over time. The first three WHOI sub−sessions and Nancy are represented by closed symbols; the fourth and fifth WHOI sub−sessions are shown by open symbols. After changing the analytical parameters and toward the end of the analysis, the data at WHOI became less scattered and stability improved significantly.

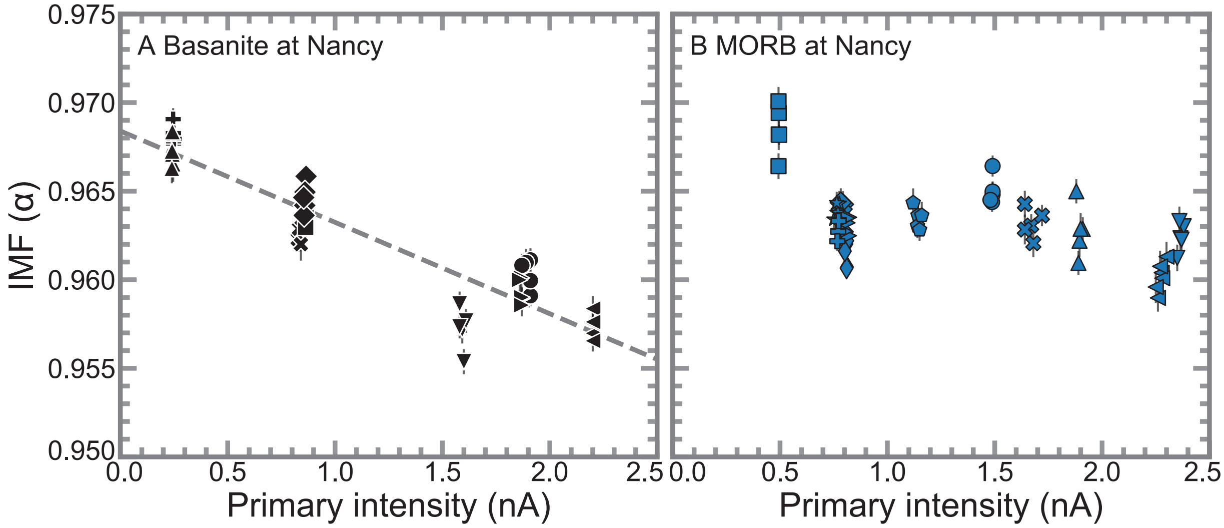

Fig. 6 Comparison between the IMF of carbon isotope ratio in alpha ($R_{measured}/R_{true}$; see 3.2.2. for the definition) and primary intensity in nA in the SIMS measurement at Nancy session (A) for Basanite reference sets and (B) for MORB reference sets. The dashed line in (A) represents the linear regression line. The same beam intensity was used to analyze the same reference material. Different symbols represent different reference glasses. In (A) for Basanite reference sets: 'CI_bas_1'-filled plus, 'CI_bas_2'-circle, 'CI_bas_3'-filled X, 'CI_bas_4'-left triangle, 'CI_bas_5'-downward triangle, 'CI_bas_6'-upward triangle, 'CI_bas_7'-right triangle, 'CI_bas_8'-square, and 'CI_bas_9'-diamond. In (B) for MORB reference sets: 'CI_Ref_6'-pentagon, 'CI_Ref_9'-filled plus, 'CI_Ref_10'-diamond, 'CI_Ref_11'-thin diamond, 'CI_Ref_15'-circle, 'CI_Ref_18'-upright triangle, 'CI_Ref_20'-filled X, 'CI_Ref_22'-downward triangle, 'CI_Ref_23'-left triangle, 'CI_Ref_25'-right triangle, 'CI_Ref_27'-star, and 'CI_Ref_28'-square.

3.2.3. Accuracy and correction

For the final IMF correction, we used the average IMF obtained from appropriate compositional reference materials. Synthetic glasses (Etna, Hawaii) and natural MORB (DR52) are used as unknowns to validate the IMF correction. The test glasses were corrected using the IMF determined from the MORB series due to their compositional proximity to MORB.

At Nancy, the average of the IMF of the MORB series was used to correct the $R_{measured}$ values for the MORB series and the test glasses. For the Basanite reference materials, a linear regression between primary beam intensity and IMF was used to correct $R_{measured}$. At WHOI, since the first and second sessions showed consistent IMF (Fig. 5), we used the average value from these two sessions. In the third session, a drift correction to the IMF was applied by performing a linear regression on the MORB reference materials over time. Finally, we used the average value from the fourth and fifth sessions to calculate the IMF during that time.

The IMF−corrected $\delta^{13}C$–values are presented in Fig. 7. There was a notable agreement between the $\delta^{13}C$–value measured by EA–IRMS (or step−heating method for DR52) and SIMS down to ~380 ppm CO_2 (DR52). After changing the analytical parameters at WHOI, the difference between $\delta^{13}C$–value measured by EA−IRMS and SIMS improved from an average of 1.4‰ (1st−3rd sub−sessions) to 1.1‰ (4th and 5th sub−sessions).

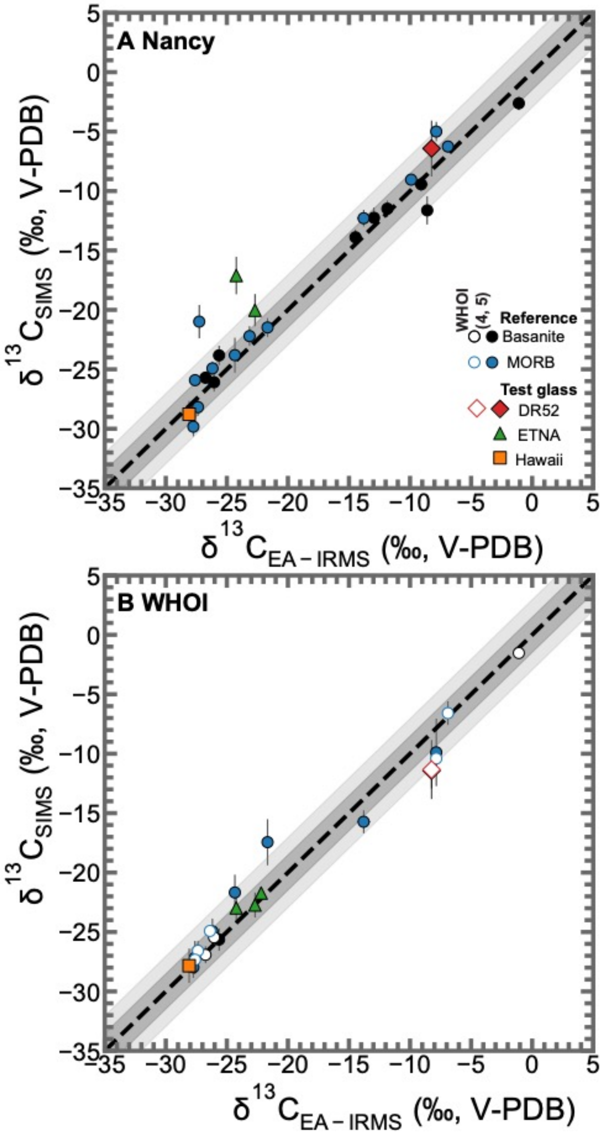

Fig. 7 Comparison between "true" δ^{13}C–value (‰, V–PDB) measured by EA−IRMS (x−axis) and IMF–corrected δ^{13}C–value (‰, V–PDB) measured by SIMS (y−axis). The dashed line is the 1:1 line. Around the dashed lines, two areas of different shading represent 1σ and 2σ errors, respectively. Note that the IMF correction is specific for the Basanite and MORB series. The MORB IMF was used for the test glasses (all of basaltic composition). Closed symbols mark Nancy and the first three sub–sessions of WHOI, while open symbols mark the fourth and fifth sub–sessions of WHOI. The error bar is 1σ for both axes.

3.3. CO_2 concentration calibration

To estimate CO_2 concentration by SIMS, we calibrated the $^{12}C/^{18}O$ ratio with the CO_2 concentrations determined by FTIR (Fig. 8). Calibration slopes were found to be consistent across the MORB and Basanite series. The systematic deviation of the NBO series (basalt to andesitic basalt) from the calibration line could be due either to the matrix effect (different matrix composition between Basanite/MORB series and NBO series) or to the use of different FTIR absorption coefficients (Shishkina et al., 2014 for Basanite/MORB series; Dixon and Pan, 1995 for NBO series). The resulting calibration showed linearity over a wide range of CO_2 abundances (380 to 12000 ppm). SIMS 1σ error on the regressions are ±24% for the Nancy session and ±21% for the WHOI session, while the average error (1σ) on the FTIR CO_2 measurements is ±11%.

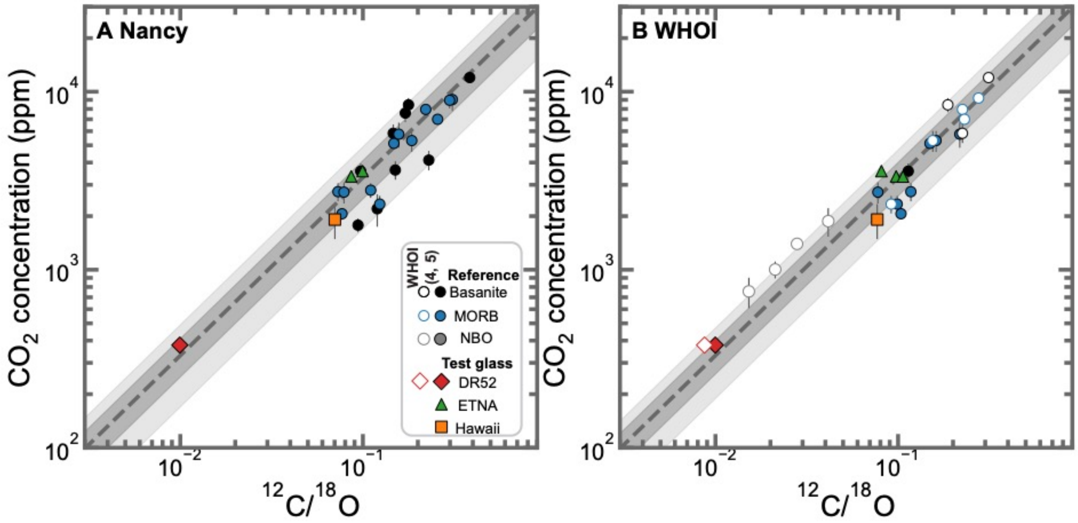

Fig. 8 $^{12}C/^{18}O$ ratio measured by SIMS at Nancy (A) and WHOI (B) versus CO_2 concentration in parts per million (ppm) measured by FTIR, except for DR52, which is measured by the step–heating method. The result from Nancy and the 1st–3rd sub–sessions from WHOI are shown with closed symbols, and the 4th and 5th sub–sessions from WHOI are shown with open symbols. Dashed lines are linear regression estimated in linear–linear space. Around the dashed lines, two differently shaded areas indicate 1σ and 2σ percent error estimated in linear–linear space. The intercept of the linear regression was forced to zero.

4. Discussion

4.1. IMF and analytical conditions

This study investigated interlaboratory reproducibility by performing analyses on ion microprobe instruments at Nancy (IMS 1270) and WHOI (IMS 1280). Significant differences in IMF were found between the two instruments. Several important differences may help explain the large variations in IMF. We used two different large–geometry SIMS models: a IMS 1270 at Nancy and a IMS 1280 at WHOI. Although we used EM detectors on both SIMS, we used two different data collection modes; the Nancy session was performed in mono–collector mode with peak switching for ^{12}C and ^{13}C, while the WHOI session was performed in peak switching multi–collector mode. In mono−collection mode, ion species are measured one after the other using a single fixed detector with changing magnetic settings. This approach prevents differential aging of the detector at high counts (^{12}C in this study) and eliminates the need for detector intercalibration. In multi−collection mode, multiple detectors record ion species simultaneously and generally provide faster measurement times, but could be affected by differential detector aging ^{12}C and ^{13}C. However, we did not experience any significant detector aging over a week−long SIMS session in multi−collection mode with applying high−voltage adjustment that can mitigate the detector aging (e.g., Hedberg et al., 2015).

Another factor contributing to the variation in IMF is the adjustment of the analytical parameters. One of the main reasons for IMF is the non−uniform distribution of secondary ions of different masses in a constant magnetic field, such as the Earth's magnetic field (e.g., Sangely et al., 2014). As a result, mechanical obstacles along the path of the secondary ions, such as entrance slits or field apertures, intercept only a portion of the heterogeneous secondary beam. This selective interception inevitably leads to deviations in the measured isotopic ratio from the natural distribution of the respective isotopes. In the fourth and fifth sub−sessions at WHOI, different analytical parameters were attempted than in the first three sub−sessions. The main parameter changes were the reduction of the field aperture and the exit slit (see 2.4.3 for details), which resulted in IMF shifts of ~3‰. We also suspect that the opening of the field aperture up to 3000 µm in the first three sub−sessions shows more scattered IMF (Fig. 5) compared to the last two sub−sessions due to the high background.

4.2. IMF and sample location on the mount

The collection efficiency of secondary ions is affected by the position of the sample in the holder. The study of oxygen isotope on zircon for instance (Kita et al., 2009) indicates that insignificant effect of the position of the sample in the holder was observed as long as the analysis spot is 6−7mm from the center of the mount. In our study, the mounts of reference materials were well–centered in the sample holder to avoid edge positions (Fig. S2).

To test the possible effect of the position of the sample in the sample holder on the IMF (e.g., Fàbrega et al., 2017), we performed two sets of analyses on the same reference materials before and after rotating the sample holder 90 degrees (sub−sessions 1 and 2 at WHOI). We found no systematic variation in IMF before and after the rotation (Fig. 5) indicating that sample position within the holder has no measurable effect on the IMF.

4.3. IMF and primary beam intensity

Variations in the primary beam current result in variable beam densities and sputtering rates, which affect the surface ionization efficiency. For instance, an increase in IMF with primary beam intensity was reported for hydrogen isotopes in silicate glass (e.g., Hauri et al., 2006).

We explored a range of beam intensities from 0.5 to 2.4nA on the Nancy IMS 1270 and found that, for the MORB series, there was no change in IMF with beam intensity (Fig. 6). For the Basanite series, however, we found a clear (R^2=0.85) correlation between beam intensity and IMF (Fig. 6A). The reason the Basanite series would show a shift in IMF with beam intensity while the MORB doesn't, over the same range of beam intensity, is unclear but further underscores the importance of using matrix−matched reference materials for this type of analysis.

An alternative way of looking at the data presented in Fig. 6 would be to consider that for the IMF of the Basanite series at Nancy is stable in the 1.5 to 2.5nA intensity range and variable at lower intensities, while for the IMF of the Basalt series at Nancy is stable in the 0.8 to 2.5nA intensity range and potentially variable at lower intensities. This further emphasizes the need for future analysis of standards and unknowns using the same beam conditions.

4.4. Drift in IMF over time

Although drift in IMF on short timescales is not always observed (Fitzsimons et al., 2000), it commonly occurs for numerous elements and matrices (e.g., Eiler et al., 1997; Hauri et al., 2006; Taracsák et al., 2021). Since the IMF is highly dependent on the chemical composition of the silicate glass (see section 4.5 and references therein), the IMF for the given reference series (MORB/Basanite) is assumed to be identical due to the nearly identical chemical compositions. Thus, any drift over time would be detectable by analyzing different glasses within the same series. With the exception of the third sub−session at WHOI, the other sub−sessions at WHOI and the Nancy session showed no systematic drift in IMF over time. The third sub−session at WHOI showed a gradual increase in IMF. Frequent high–voltage adjustments to the detectors to maintain the pulse–height distribution curve can mitigate the IMF drift (e.g., Hedberg et al., 2015), which we applied to WHOI analyses. However, it is recommended that drift should be monitored by inserting analyses of reference materials at regular intervals during the measurements, as well as at the beginning and end of the analytical session (e.g., Fitzsimons et al., 2000; Hartley et al., 2012; Peterson et al., 2023).

4.5. IMF and glass composition

Across various isotopes, the IMF in silicate glasses has been observed to vary as a function of compositional indices, for example, SiO_2 wt% (De Hoog and EIMF, 2018 for Li; Dubinina et al., 2021, Gurenko et al., 2001, Hartley et al., 2012 for O), H_2O and Al_2O_3 abundances (Hauri et al., 2006; Sobolev et al., 2019), SiO_2, Al_2O_3 and K_2O moles (Manzini et al., 2017 for Cl). To further explore the variation in IMF of carbon isotope across matrix compositions, we examined the Basanite and NBO series in the WHOI 5th sub−session, which provide a range of compositions from basanite to basaltic andesite (Fig. 1) and are analyzed using the same analytical parameters except for beam intensity (Basanite−1nA and NBO−5nA). Table 3 was generated to show correlation coefficients of different compositional parameters with IMF.

IMF shows a negative correlation with mole fractions of SiO_2, Al_2O_3, and H_2O, while other cations show a positive correlation. This relationship may be due to differences in the efficiency of kinetic energy transfer from primary to secondary ions depending on the matrix composition (Eiler et al., 1997; Hauri et al., 2006). Efficient energy transfer in heavier matrices results in less fractionation from the true $^{13}C/^{12}C$ and hence higher IMF in alpha. This may also explain the negative correlation observed for lighter elements, especially H_2O. For H_2O, although H_2O is known to suppress carbon ionization in basaltic glass (e.g., Behrens et al., 2004; Moussallam et al., 2024; H_2O ranges 0.0–6.8 wt%), the limited H_2O range (0.8–1.7 wt% for MORB and Basanite series) in our study prevents confirmation of IMF variation with H_2O.

It remains challenging to determine the precise effects of individual elements on IMF due to limited data and compositional variations. Further detailed investigation of the relationship between IMF and composition is needed, however, underscoring the importance of selecting a reference material that closely matches the composition of the sample of interest.

Table 3
Correlation and determination coefficient between various compositional indices and IMF in alpha for NBO series and Basanite results from WHOI 5th sub−session. The residual error (relative root mean squared error) is also shown in permil. The list order is sorted from highest R^2 to lowest R^2.

Compositional index	Correlation coefficient (R)	Determination coefficient (R^2)	Relative Root Mean Squared Error (RRMSE, ‰)
XP_2O_5	0.92	0.85	0.76
Density (hydrous)	0.92	0.84	0.78
XFeO	0.91	0.84	0.78
XNa_2O	0.91	0.82	0.81
Alkalinity	0.89	0.80	0.87
XCaO	0.89	0.80	0.87
$XSiO_2$	-0.89	0.79	0.89
$XTiO_2$	0.88	0.78	0.92
XMgO	0.88	0.77	0.92
NBO/T (hydrous)*	0.88	0.77	0.93
XH_2O	-0.87	0.76	0.96
XK_2O	0.85	0.73	1.00
XCO_2	0.85	0.72	1.03
XAl_2O_3	-0.75	0.56	1.29
XMnO	0.72	0.52	1.34

*calculated according to Iacono–Marziano et al. (2012)

4.6. Implication of this study

SIMS offers an advantage over bulk analysis for δ^{13}C−value measurement by avoiding potential contamination problems and allowing *in situ* analysis at the micron scale. Achieving smaller spots with high precision is an imperative goal for the analysis of small objects such as melt inclusions. While previous attempts have achieved reproducibility of 2–3‰ with a 40µm primary beam diameter at up to 50nA (Hauri et al., 2002), such dimensions may not be suitable for all samples. While higher beam intensities offer potentially higher precision, they also increase the beam diameter and risk charging the sample surface. In particular, we would like to emphasize that in our study, both internal and external precision levels typically below ±1.0‰ were achieved using a 10µm diameter spot size and less than 5nA for CO_2 concentrations down to 1800±200 ppm.

4.7. Recommendation for δ^{13}C analyses in silicate glasses by SIMS

The mount analyzed at the Ion Microprobe facility at the CNRS−CRPG Nancy is available to users there, and the mount analyzed at WHOI will be deposited at the Smithsonian Museum of Natural History, where it will be available to any researcher upon request. Given the finite amount of material available on these two mounts, we ask future users to treat them with care, limiting the number of analyses to what is strictly necessary for their analyses, but also limiting the beam intensity and spot size used for the analysis.

Our recommendation for future analyses of $\delta^{13}C$ in silicate glasses by SIMS is the following:

1. Reduce background: To reduce background interference from the mount itself, samples should be mounted in indium or Sn−Bi alloy (e.g., Cui et al., 2024; Zhang et al., 2018). Thoroughly clean off any crystal bond, acetone deposits, and other contaminants in your samples before mounting them to minimize unwanted signals (e.g., use of dichloromethane to remove any organic material on the surface; Mattey et al., 1989). Try to obtain the best possible quality results at polishing. Cracks, cavities, caverns or any other defects resulting from insufficient polishing usually contain rests of fiber and abrasive materials and present a source of huge contamination by carbon that is nearly impossible to eliminate by cleaning. We recommend that you never use diamond−based polishing materials for sample preparation, but instead use corundum abrasives (see similar recommendations in Rose-Koga et al., 2021). We also recommend that samples should never have been C−coated before attempting this type of analysis. C−coating removal, even with a few microns of polishing, can never guarantee complete removal of C nanoparticles from the sample surface. In addition, it is recommended to use sufficient pre–sputtering time for surface cleaning preparation to reduce background (120 seconds or more). However, excessively long pre–sputtering or numerous analysis cycles should be avoided to prevent targeting inaccurate location or uneven surface. Previous effort has used a 400μm field aperture to reduce background (Hauri et al., 2002), but this approach also attenuates the signal as well. In our study, we reduced ^{12}C background intensity by a factor of 10 on the olivine blank as a result of adjusting the field aperture size from 3000μm to 1500μm. It is strongly recommended that background, which can be assessed using olivine, Suprasil (or any CO_2−free mineral), or devolatilized glass mounted on the same mount as the unknown samples, be measured as blank at all analytical setups including beam currents throughout the session to keep track of carbon background contribution.

2. Optimize signal: As shown in Fig. 3, the higher the count rate, the better the precision. The relationship, however, is not linear such that very high−count rates (>300,000 cps on ^{12}C), liable to damage the detector are not recommended. Instead, it is recommended to aim for

a count rate of around 300,000 cps on ^{12}C (3,000 cps on ^{13}C). To do so requires some *a priori* knowledge of the CO_2 content in the unknown glass in order to choose a beam current that would yield this count rate. The best−case scenario would be to analyze the unknown first for CO_2 content under standard SIMS volatile analyses conditions prior to attempting $\delta^{13}C$ analyses. With small melt inclusions with limited analyzable surface however this may not be practical. An alternative is to check the intensity of the ^{12}C signal on each unknown first to decide under which beam condition to run the $\delta^{13}C$ analyze. Note that when employing this method care should be taken to still pre−sputter the area in which the beam signal intensity is being measured to avoid any surface contamination effect. It is also recommended to increase the count times or the number of cycles to achieve better precision, but too many analysis cycles should be avoided for the same reasons as for too long pre−sputtering.

3. Characterize IMF in detail: We recommend analyzing multiple (at least five) reference materials of matrix−matched composition with your unknown in order to properly constrain the IMF during your analytical session. In addition, we recommend monitoring for drift by measuring the reference materials at the beginning and end of the session as well as by periodically performing repeated analysis on a reference material during the session. Finally, if using multiple primary beam intensities on your unknown, we recommend testing the effect of this range of primary beam intensities on the reference material of matrix−matched composition. The list of "best" reference materials, selected based on their small difference between internal and external precision and their agreement with the calibration line for both $\delta^{13}C$−values and CO_2 concentrations at Nancy or WHOI, is shown in Table S8. It should be noted however that any of the 31 reference materials are suitable for use as reference material across the compositional, CO_2 concentration and $\delta^{13}C$ range they cover.

5. Conclusion

In this study, we characterized 30 experimental glasses of MORB and Basanite compositions and 1 natural basalt intended to serve as international reference materials for $\delta^{13}C$−value measurements by SIMS. We achieved internal precision in the order of ±1.1‰ (minimum ±0.3‰) for spot sizes between 10 to 20μm. This significant development makes possible the analysis of small samples such as melt inclusions. This precision was achieved by adjusting the primary beam intensity to maintain a ^{12}C signal around 300,000 cps. We demonstrated that our reference materials are homogeneous in $\delta^{13}C$–values and allow characterization of instrumental mass fractionation (which can vary widely between instruments and analytical conditions) with an average reproducibility of ±1.0‰ for CO_2 concentration down to 1800±200 ppm. The reference materials are now available at the CNRS–CRPG ion microprobe facility in Nancy and will be deposited at the Smithsonian National Museum of Natural History, where they will be freely available on loan to any researcher.

Data availability

All data used in this study and figure, including raw analysis data, are available in the manuscript and in the Supplementary Table.

Author contributions

Initial study design: H.L., Y.M.
Experiments: H.L., Y.M.
FTIR: H.L.
EA–IRMS: H.L.
EMPA: H.L.
SIMS (Nancy): Y.M., E.R.K., L.P., J.V., N.B., A.G., É.D.
SIMS (WHOI): H.L., Y.M., B.M., G.G.
Writing and interpretation: All authors, first draft H.L., Y.M.

Declaration of competing interest

The authors declare that they have no known competing financial interests or personal relationships that could have appeared to influence the work reported in this paper.

Declaration of generative AI in scientific writing

During the preparation of this work the authors used DeepL in order to improve readability and language. After using this tool, the authors reviewed and edited the content as needed and take full responsibility for the content of the publication.

Acknowledgment

We are very grateful for the five anonymous reviewers for their comments and suggestions. Special thanks to Cyril Aubaud for providing the DR52 sample. We would also like to thank Céline Martin (AMNH) for her assistance with the microprobe analysis and Wei Huang for her valuable contributions to the analysis with the elemental analyser (LDEO). Funding: This work is part of Hyun Joo Lee's Ph.D. thesis, supported by the FORED (Foundation for Overseas Resources Development) scholarship program. We thank Marion Le Voyer for sharing her log−books and trial reports from 2012−2013, when she first started carbon isotope investigation by SIMS with Erik Hauri. Glenn Gaetani was supported by the *Independent Research & Development Program at WHOI.*

References

Barker, C., Torkelson, B.E., 1975. Gas adsorption on crushed quartz and basalt. Geochimica et Cosmochimica Acta 39, 212–218. https://doi.org/10.1016/0016-7037(75)90173-8

Barnes, J.D., Sharp, Z.D., 2006. Achlorine isotope study of DSDP/ODP serpentinized ultramafic rocks: Insights into the serpentinization process. Chemical Geology 228, 246–265. https://doi.org/10.1016/j.chemgeo.2005.10.011

Behrens, H., Ohlhorst, S., Holtz, F., Champenois, M., 2004. CO_2 solubility in dacitic melts equilibrated with H_2O-CO_2 fluids: Implications for modeling the solubility of CO_2 in silicic melts. Geochimica et Cosmochimica Acta 68, 4687–4703. https://doi.org/10.1016/j.gca.2004.04.019

Bourgue, E., Richet, P., 2001. The effects of dissolved CO_2 on the density and viscosity of silicate melts: a preliminary study. Earth and Planetary Science Letters 193, 57–68. https://doi.org/10.1016/S0012-821X(01)00491-5

Cartigny, P., Pineau, F., Aubaud, C., Javoy, M., 2008. Towards a consistent mantle carbon flux estimate: Insights from volatile systematics (H_2O/Ce, δD, CO_2/Nb) in the North Atlantic mantle (14°N and 34°N). Earth and Planetary Science Letters 265, 672–685. https://doi.org/10.1016/j.epsl.2007.11.011

Cocker, J.D., Griffin, B.J., Muehlenbachs, K., 1982. Oxygen and carbon isotope evidence for seawater-hydrothermal alteration of the Macquarie Island ophiolite. Earth and Planetary Science Letters 61, 112–122. https://doi.org/10.1016/0012-821X(82)90043-7

Craig, H., 1957. Isotopic standards for carbon and oxygen and correction factors for mass-spectrometric analysis of carbon dioxide. Geochimica et Cosmochimica Acta 12, 133–149. https://doi.org/10.1016/0016-7037(57)90024-8

Cui, Z., Xia, X.-P., Yang, Q., Zhang, K., Yang, X., Lai, C.-K., Zhang, W.-F., Zhang, Y.-Q., Yang, Y.-N., 2024. Ultralow H_2O content analysis with a large-geometry secondary ion mass spectrometer. J. Anal. At. Spectrom. 39, 1070–1076. https://doi.org/10.1039/D3JA00422H

De Hoog, J.C.M., EIMF, 2018. Matrix Effects During SIMS Measurement of the Lithium Mass Fractions of Silicate Glasses: Correction Procedures and Updated Preferred Values of

Reference Materials. Geostandard Geoanalytic Res 42, 513–522. https://doi.org/10.1111/ggr.12237

Dixon, J.E., Pan, V., 1995. Determination of the molar absorptivity of dissolved carbonate in basanitic glass. American Mineralogist 80, 1339–1342. https://doi.org/10.2138/am-1995-11-1224

Dubinina, E., Borisov, A., Wiedenbeck, M., Rocholl, A., 2021. SIMS oxygen isotope matrix effects in silicate glasses: Quantifying the role of chemical composition. Chemical Geology 578, 120322. https://doi.org/10.1016/j.chemgeo.2021.120322

Eiler, J.M., Graham, C., Valley, J.W., 1997. SIMS analysis of oxygen isotopes: matrix effects in complex minerals and glasses. Chemical Geology 138, 221–244. https://doi.org/10.1016/S0009-2541(97)00015-6

Fàbrega, C., Parcerisa, D., Rossell, J.M., Gurenko, A., Franke, C., 2017. Predicting instrumental mass fractionation (IMF) of stable isotope SIMS analyses by response surface methodology (RSM). J. Anal. At. Spectrom. 32, 731–748. https://doi.org/10.1039/C6JA00397D

Fitzsimons, I.C.W., Harte, B., Clark, R.M., 2000. SIMS stable isotope measurement: counting statistics and analytical precision. Mineral. mag. 64, 59–83. https://doi.org/10.1180/002646100549139

Gurenko, A.A., Chaussidon, M., Schmincke, H.-U., 2001. Magma ascent and contamination beneath one intraplate volcano: evidence from S and O isotopes in glass inclusions and their host clinopyroxenes from Miocene basaltic hyaloclastites southwest of Gran Canaria (Canary Islands). Geochimica et Cosmochimica Acta 65, 4359–4374. https://doi.org/10.1016/S0016-7037(01)00737-2

Hartley, M.E., Thordarson, T., Taylor, C., Fitton, J.G., Eimf, 2012. Evaluation of the effects of composition on instrumental mass fractionation during SIMS oxygen isotope analyses of glasses. Chemical Geology 334, 312–323. https://doi.org/10.1016/j.chemgeo.2012.10.027

Hauri, E., Wang, J., Dixon, J.E., King, P.L., Mandeville, C., Newman, S., 2002. SIMS analysis of volatiles in silicate glasses. Chemical Geology 183, 99–114. https://doi.org/10.1016/S0009-2541(01)00375-8

Hauri, E.H., Shaw, A.M., Wang, J., Dixon, J.E., King, P.L., Mandeville, C., 2006. Matrix effects in hydrogen isotope analysis of silicate glasses by SIMS. Chemical Geology 235, 352–365. https://doi.org/10.1016/j.chemgeo.2006.08.010

Hedberg, P.M.L., Peres, P., Fernandes, F., Renaud, L., 2015. Multiple ion counting measurement strategies by SIMS – a case study from nuclear safeguards and forensics. J. Anal. At. Spectrom. 30, 2516–2524. https://doi.org/10.1039/C5JA00382B

Iacono-Marziano, G., Morizet, Y., Le Trong, E., Gaillard, F., 2012. New experimental data and semi-empirical parameterization of H_2O–CO_2 solubility in mafic melts. Geochimica et Cosmochimica Acta 97, 1–23. https://doi.org/10.1016/j.gca.2012.08.035

Ihinger, P.D., Hervig, R.L., McMillan, P.F., 1994. Chapter 2. ANALYTICAL METHODS FOR VOLATILES IN GLASSES, in: Carroll, M.R., Holloway, J.R. (Eds.), Volatiles in Magmas. De Gruyter, pp. 67–122. https://doi.org/10.1515/9781501509674-008

Kita, N.T., Ushikubo, T., Fu, B., Valley, J.W., 2009. High precision SIMS oxygen isotope analysis and the effect of sample topography. Chemical Geology 264, 43–57. https://doi.org/10.1016/j.chemgeo.2009.02.012

Lee, H.J., Moussallam, Y., Aubaud, C., Iacono-Marziano, G., Hammond, K., Ebel, D., 2024. Carbon isotope fractionation between CO_2 and carbon in silicate melts at high temperature. https://doi.org/10.31223/X5NH6R

Lesher, C.E., Spera, F.J., 2015. Thermodynamic and Transport Properties of Silicate Melts and Magma, in: The Encyclopedia of Volcanoes. Elsevier, pp. 113–141. https://doi.org/10.1016/B978-0-12-385938-9.00005-5

Loewen, M.W., Graham, D.W., Bindeman, I.N., Lupton, J.E., Garcia, M.O., 2019. Hydrogen isotopes in high $^3He/^4He$ submarine basalts: Primordial vs. recycled water and the veil of mantle enrichment. Earth and Planetary Science Letters 508, 62–73. https://doi.org/10.1016/j.epsl.2018.12.012

Longpré, M.-A., Stix, J., Klügel, A., Shimizu, N., 2017. Mantle to surface degassing of carbon- and sulphur-rich alkaline magma at El Hierro, Canary Islands. Earth and Planetary Science Letters 460, 268–280. https://doi.org/10.1016/j.epsl.2016.11.043

Maevaray, R., 2017. Caractérisation des éléments volatils dans une série de basaltes de ride de l'Océan Indien. Université Paris Diderot.

Manzini, M., Bouvier, A.-S., Barnes, J.D., Bonifacie, M., Rose-Koga, E.F., Ulmer, P., Métrich, N., Bardoux, G., Williams, J., Layne, G.D., Straub, S., Baumgartner, L.P., John, T., 2017. SIMS chlorine isotope analyses in melt inclusions from arc settings. Chemical Geology 449, 112–122. https://doi.org/10.1016/j.chemgeo.2016.12.002

Mathez, E.A., Delaney, J.R., 1981. The nature and distribution of carbon in submarine basalts and peridotite nodules. Earth and Planetary Science Letters 56, 217–232. https://doi.org/10.1016/0012-821X(81)90129-1

Mattey, D.P., 1991. Carbon dioxide solubility and carbon isotope fractionation in basaltic melt. Geochimica et Cosmochimica Acta 55, 3467–3473. https://doi.org/10.1016/0016-7037(91)90508-3

Mattey, D.P., Carr, R.H., Wright, I.P., Pillinger, C.T., 1984. Carbon isotopes in submarine basalts. Earth and Planetary Science Letters 70, 196–206. https://doi.org/10.1016/0012-821X(84)90005-0

Mattey, D.P., Exley, R.A., Pillinger, C.T., 1989. Isotopic composition of CO_2 and dissolved carbon species in basalt glass. Geochimica et Cosmochimica Acta 53, 2377–2386. https://doi.org/10.1016/0016-7037(89)90359-1

Médard, E., Grove, T.L., 2008. The effect of H_2O on the olivine liquidus of basaltic melts: experiments and thermodynamic models. Contrib Mineral Petrol 155, 417–432. https://doi.org/10.1007/s00410-007-0250-4

Moussallam, Y., Georgeais, G., Rose-Koga, E.F., Koga, K.T., Hartley, M.E., Scaillet, B., Oppenheimer, C., Peters, N., 2023. CO_2 -Undersaturated Melt Inclusions From the South West Indian Ridge Record Surprisingly Uniform Redox Conditions. Geochem Geophys Geosyst 24, e2023GC011235. https://doi.org/10.1029/2023GC011235

Moussallam, Y., Longpré, M.-A., McCammon, C., Gomez-Ulla, A., Rose-Koga, E.F., Scaillet, B., Peters, N., Gennaro, E., Paris, R., Oppenheimer, C., 2019. Mantle plumes are oxidised. Earth and Planetary Science Letters 527, 115798. https://doi.org/10.1016/j.epsl.2019.115798

Moussallam, Y., Towbin, W., Plank, T., Bureau, H., Khodja, H., Guan, Y., Ma, C., Baker, M., Stolper, E., Naab, F., Monteleone, B., Gaetani, G., Lee, H.J., Ding, S., Shi, S., Rose-Koga, E., 2024. ND70 series basaltic glass reference materials for volatile element (H_2O,

CO_2, S, Cl, F) analysis and the C ionisation efficiency suppression effect of water in silicate glasses in SIMS analysis. https://doi.org/10.31223/X5QQ4P

Nichols, A.R.L., Wysoczanski, R.J., 2007. Using micro-FTIR spectroscopy to measure volatile contents in small and unexposed inclusions hosted in olivine crystals. Chemical Geology 242, 371–384. https://doi.org/10.1016/j.chemgeo.2007.04.007

Peterson, L.D., Newcombe, M.E., Alexander, C.M.O., Wang, J., Sarafian, A.R., Bischoff, A., Nielsen, S.G., 2023. The H_2O content of the ureilite parent body. Geochimica et Cosmochimica Acta 340, 141–157. https://doi.org/10.1016/j.gca.2022.10.036

Pineau, F., Javoy, M., 1983. Carbon isotopes and concentrations in mid-oceanic ridge basalts. Earth and Planetary Science Letters 62, 239–257. https://doi.org/10.1016/0012-821X(83)90087-0

Rose-Koga, E.F., Bouvier, A.-S., Gaetani, G.A., Wallace, P.J., Allison, C.M., Andrys, J.A., Angeles De La Torre, C.A., Barth, A., Bodnar, R.J., Bracco Gartner, A.J.J., Butters, D., Castillejo, A., Chilson-Parks, B., Choudhary, B.R., Cluzel, N., Cole, M., Cottrell, E., Daly, A., Danyushevsky, L.V., DeVitre, C.L., Drignon, M.J., France, L., Gaborieau, M., Garcia, M.O., Gatti, E., Genske, F.S., Hartley, M.E., Hughes, E.C., Iveson, A.A., Johnson, E.R., Jones, M., Kagoshima, T., Katzir, Y., Kawaguchi, M., Kawamoto, T., Kelley, K.A., Koornneef, J.M., Kurz, M.D., Laubier, M., Layne, G.D., Lerner, A., Lin, K.-Y., Liu, P.-P., Lorenzo-Merino, A., Luciani, N., Magalhães, N., Marschall, H.R., Michael, P.J., Monteleone, B.D., Moore, L.R., Moussallam, Y., Muth, M., Myers, M.L., Narváez, D.F., Navon, O., Newcombe, M.E., Nichols, A.R.L., Nielsen, R.L., Pamukcu, A., Plank, T., Rasmussen, D.J., Roberge, J., Schiavi, F., Schwartz, D., Shimizu, K., Shimizu, K., Shimizu, N., Thomas, J.B., Thompson, G.T., Tucker, J.M., Ustunisik, G., Waelkens, C., Zhang, Y., Zhou, T., 2021. Silicate melt inclusions in the new millennium: A review of recommended practices for preparation, analysis, and data presentation. Chemical Geology 570, 120145. https://doi.org/10.1016/j.chemgeo.2021.120145

Sakai, H., Casadevall, T.J., Moore, J.G., 1982. Chemistry and isotope ratios of sulfur in basalts and volcanic gases at Kilauea volcano, Hawaii. Geochimica et Cosmochimica Acta 46, 729–738. https://doi.org/10.1016/0016-7037(82)90024-2

Sangely, L., Boyer, B., De Chambost, E., Valle, N., Audinot, J.-N., Ireland, T., Wiedenbeck, M., Aléon, J., Jungnickel, H., Barnes, J.-P., Bienvenu, P., Breuer, U., 2014. Secondary Ion Mass Spectrometry, in: Prohaska, T., Irrgeher, J., Zitek, A., Jakubowski, N. (Eds.), Sector Field Mass Spectrometry for Elemental and Isotopic Analysis. The Royal Society of Chemistry, pp. 439–499. https://doi.org/10.1039/9781849735407-00439

Schuhmacher, M., Fernandes, F., De Chambost, E., 2004. Achieving high reproducibility isotope ratios with the Cameca IMS 1270 in the multicollection mode. Applied Surface Science 231–232, 878–882. https://doi.org/10.1016/j.apsusc.2004.03.157

Shimizu, K., Ushikubo, T., Murai, T., Matsu'ura, F., Ueno, Y., 2019. *In situ* analyses of hydrogen and sulfur isotope ratios in basaltic glass using SIMS. Geochem. J. 53, 195–207. https://doi.org/10.2343/geochemj.2.0559

Shishkina, T.A., Botcharnikov, R.E., Holtz, F., Almeev, R.R., Jazwa, A.M., Jakubiak, A.A., 2014. Compositional and pressure effects on the solubility of H_2O and CO_2 in mafic melts. Chemical Geology 388, 112–129. https://doi.org/10.1016/j.chemgeo.2014.09.001

Slodzian, G., Lorin, J.C., Havette, A., 1980. Isotopic effect on the ionization probabilities in secondary ion emission. J. Phyique Lett. 41, 555–558. https://doi.org/10.1051/jphyslet:019800041023055500

Sobolev, A.V., Asafov, E.V., Gurenko, A.A., Arndt, N.T., Batanova, V.G., Portnyagin, M.V., Garbe-Schönberg, D., Wilson, A.H., Byerly, G.R., 2019. Deep hydrous mantle reservoir provides evidence for crustal recycling before 3.3 billion years ago. Nature 571, 555–559. https://doi.org/10.1038/s41586-019-1399-5

Taracsák, Z., Neave, D.A., Beaudry, P., Gunnarsson-Robin, J., Burgess, R., Edmonds, M., Halldórsson, S.A., Longpré, M.-A., Ono, S., Ranta, E., Stefánsson, A., Turchyn, A.V., Eimf, Hartley, M.E., 2021. Instrumental mass fractionation during sulfur isotope analysis by secondary ion mass spectrometry in natural and synthetic glasses. Chemical Geology 578, 120318. https://doi.org/10.1016/j.chemgeo.2021.120318

United States Geological Survey Reston Stable Isotope Laboratory, 2011, Report of Stable Isotopic Composition Reference Material USGS41 (Carbon and Nitrogen Isotopes in L-glutamic Acid), https://d9-wret.s3.us-west-2.amazonaws.com/assets/palladium/production/s3fs-public/atoms/files/USGS41_0.pdf (accessed 23 Apr 2024)

United States Geological Survey Reston Stable Isotope Laboratory, 2019a, Report of Stable Isotopic Composition Reference Material USGS24 (Carbon Isotopes in Graphite), https://d9-wret.s3.us-west-2.amazonaws.com/assets/palladium/production/s3fs-public/media/files/USGS24.pdf (accessed 23 Apr 2024)

United States Geological Survey Reston Stable Isotope Laboratory, 2019b, Report of Stable Isotopic Composition Reference Material USGS40 (Carbon and Nitrogen Isotopes in L-glutamic Acid), https://d9-wret.s3.us-west-2.amazonaws.com/assets/palladium/production/s3fs-public/atoms/files/USGS40_0.pdf (accessed 23 Apr 2024)

Valley, J.W., Graham, C.M., 1991. Ion microprobe analysis of oxygen isotope ratios in granulite facies magnetites: diffusive exchange as a guide to cooling history. Contr. Mineral. and Petrol. 109, 38–52. https://doi.org/10.1007/BF00687199

Zhang, W., Xia, X., Zhang, Y., Peng, T., Yang, Q., 2018. A novel sample preparation method for ultra-high vacuum (UHV) secondary ion mass spectrometry (SIMS) analysis. J. Anal. At. Spectrom. 33, 1559–1563. https://doi.org/10.1039/C8JA00087E